

**Pressure-induced structural and semiconductor-semiconductor transitions in  $\text{Co}_{0.5}\text{Mg}_{0.5}\text{Cr}_2\text{O}_4$** S. Rahman,<sup>1,2</sup> Hajra Saqib,<sup>2</sup> Jinbo Zhang,<sup>3</sup> D. Errandonea,<sup>4</sup> C. Menéndez,<sup>5</sup> C. Cazorla,<sup>5</sup> Sudeshna Samanta,<sup>2</sup> Xiaodong Li,<sup>6</sup> Junling Lu,<sup>1,\*</sup> and Lin Wang<sup>2,†</sup><sup>1</sup>*Department of Chemical Physics, University of Science and Technology of China, Hefei, China*<sup>2</sup>*Center for High Pressure Science and Technology Advanced Research, Shanghai 201203, China*<sup>3</sup>*College of Physical Science and Technology, Yangzhou University, Yangzhou 225002, China*<sup>4</sup>*Departamento de Física Aplicada-ICMUV, MALTA Consolider Team, Universidad de Valencia, Edificio de Investigación, C/Dr. Moliner 50, Burjassot, 46100 Valencia, Spain*<sup>5</sup>*School of Materials Science and Engineering, UNSW Australia, Sydney NSW 2052, Australia*<sup>6</sup>*Institute of High Energy Physics, Chinese Academy of Sciences, Beijing 100049, China*

(Received 2 February 2018; revised manuscript received 23 April 2018; published 10 May 2018)

The effect of pressure on the structural, vibrational, and electronic properties of Mg-doped Cr bearing spinel  $\text{Co}_{0.5}\text{Mg}_{0.5}\text{Cr}_2\text{O}_4$  was studied up to 55 GPa at room-temperature using x-ray diffraction, Raman spectroscopy, electrical transport measurements, and *ab initio* calculations. We found that the ambient-pressure phase is cubic (spinel-type,  $Fd\bar{3}m$ ) and underwent a pressure-induced structural transition to a tetragonal phase (space group  $I\bar{4}m2$ ) above 28 GPa. The *ab initio* calculation confirmed this first-order phase transition. The resistivity of the sample decreased at low pressures with the existence of a low-pressure (LP) phase and started to increase with the emergence of a high-pressure (HP) phase. The temperature dependent resistivity experiments at different pressures illustrated the wide band gap semiconducting nature of both the LP and HP phases with different activation energies, suggesting a semiconductor-semiconductor transition at HP. No evidence of chemical decomposition or a semiconductor-metal transition was observed in our studies.

DOI: [10.1103/PhysRevB.97.174102](https://doi.org/10.1103/PhysRevB.97.174102)**I. INTRODUCTION**

The diverse spinel compounds with an unfilled *d* orbital are very interesting due to their magnetoelastic coupling, charge ordering, complex structural, and electronic properties [1–3]. Due to these rich sets of characteristics, the spinel oxides (ferrites, chromites, and cobaltites) are very useful in modern technologies such as electromagnetic sensors and spintronics [2,4]. In addition, they are commercially important refractory materials for some technological applications such as secondary refining, nonferrous metal metallurgy, cement rotary kilns, thermocouple protection tubes, coal gasifier lining, and glass furnaces [5–8]. The complex spinel materials generally adopt the formula  $\text{XY}_2\text{Z}_4$ , where  $Y = \text{Cr, Fe, Al}$  with two distinct coordination polyhedra for the metal atoms (cations) located at the tetrahedral [X] and octahedral [Y] sites in an [X]:[Y] mole ratio of 1:2, while generally the anions are ( $Z = \text{O, S, Se, etc.}$ ). In most spinels, the anions are oxygen atoms (oxospinel) [9]. If  $\text{Cr}^{+3}$  ions reside at the *Y* sites, the material is known as chromite, and if  $\text{Fe}^{+3}$  ions are at the *Y* sites, the material will be ferrite. Categorically, spinels are normal and inverse on the basis of their cation distribution, such as  $[\text{X}]^{\text{tet}}[\text{Y}_2]^{\text{oct}}\text{O}_4$  and  $[\text{Y}]^{\text{tet}}[\text{XY}]^{\text{oct}}\text{O}_4$ , respectively. The Cr bearing spinel can be very useful for catalysts, data storage, dye, magnetocapacitive devices, and as a substrate for film growth.

Magnesiocromite ( $\text{MgCr}_2\text{O}_4$ ) and cobalt chromite ( $\text{CoCr}_2\text{O}_4$ ) are both normal spinel structures and *p*-type semiconductors [10], but  $\text{CoCr}_2\text{O}_4$  is ferromagnetic at low temperature while  $\text{MgCr}_2\text{O}_4$  is antiferromagnetic. Kamran *et al.* reported that Mg doping can significantly affect the structural, magnetic, and dielectric properties of  $\text{CoCr}_2\text{O}_4$  nanoparticles [11]. Earlier, a structural transition from cubic to tetragonal phase for  $\text{Co}_{0.5}\text{Cu}_{0.5}\text{Cr}_2\text{O}_4$  was observed and attributed to substitution by the Jahn-Teller (JT) ion ( $\text{Cu}^{2+}$ ) [12] causing a cooperative Jahn-Teller distortion. In another study, Bush *et al.* measured the dielectric properties of Ni-doped  $\text{CoCr}_2\text{O}_4$  and observed an increase in the magnitudes of  $\tan \delta$  (dielectric loss tangent) and  $1/\rho$  (conductivity) by increasing the Ni concentration. These studies show that doping has a significant role in controlling the magnetic and electric transport properties of  $\text{CoCr}_2\text{O}_4$  nanoparticles. Moreover, the physical properties of the Cr-based spinel change due to the interaction between the *X* and *Y* sites and dispersion of trivalent and divalent ions between these sites.  $\text{CoCr}_2\text{O}_4$  is a positive spinel structure, where the Co and Cr ions occupy the tetrahedral and octahedral sites, respectively. Although the ionic radius of  $\text{Mg}^{2+}$  (0.65 Å) is smaller than  $\text{Co}^{2+}$  (0.72 Å) [11,13], the Mg ions can replace the cobalt ions that occupy the tetrahedral position [11,13], which can reduce their magnetic/electric anisotropy and control their structural stability. Due to the intimate coupling between these physical properties, these materials have been studied extensively over the years. Given these strong interrelations among the structural, vibrational, magnetic, and electronic degrees of freedom, the physical properties of the spinel can

\*Corresponding author: Junling@ustc.edu.cn

†Author to whom all correspondence should be addressed: wanglin@hpcstar.ac.cn

be tuned externally by perturbations such as temperature ( $T$ ) and pressure ( $P$ ). Pressure, an independent thermal dynamic parameter, is an especially powerful tool for changing the physical properties of the spinel material. In our previous study, we observed a phase transition from a cubic to orthorhombic structure together with a Mott-insulator–metal transition for  $\text{Zn}_{0.2}\text{Mg}_{0.8}\text{Fe}_2\text{O}_4$  at high pressure (HP) [9]. In another HP study of the Cr-based spinel, pressure enhanced all magnetic ordering temperatures  $T_c$ ,  $T_L$ , and  $T_S$  at almost similar rates [14]. Mao *et al.* observed an exponential increase in conductivity and redshift absorption in the spinel under pressure, which suggests that the band gap in spinels can be tuned by pressure [15].

Recently, doping of the Cr-based spinel with different divalent ions (e.g.,  $\text{Ni}^{2+}$ ,  $\text{Cu}^{2+}$ ,  $\text{Zn}^{2+}$ ,  $\text{Co}^{2+}$ , and  $\text{Mg}^{2+}$ ) to make compounds such as  $\text{Co}_x\text{Mg}_{1-x}\text{Cr}_2\text{O}_4$  has gained interest. However, their physical properties have been explored less under pressure. Furthermore, there is a complete lack of high-pressure data on electrical resistivity measurements for the spinel of this family, except  $\text{FeCr}_2\text{O}_4$  [16], where a three orders of magnitude resistivity decrease was associated with a structural transition. In this article, we probe the occurrence of the HP-induced structural and semiconductor-semiconductor transitions in  $\text{Mg}_x\text{Co}_{1-x}\text{Cr}_2\text{O}_4$  ( $x = 0.5$ ) by synchrotron x-ray diffraction (XRD), Raman spectroscopy, resistivity measurements, and *ab initio* calculations. This compound's dielectric properties are improved for nanoparticles with similar Mg concentrations, which can be attributed to variations in local magnetic exchange interactions [3,11]. A phase transition from cubic to tetragonal was observed above  $\sim 28$  GPa, which was further confirmed by HP Raman spectra and *ab initio* calculations. Our HP resistivity measurements confirm that the low- and high-pressure phases are wide-band-gap semiconductors, indicating a semiconductor-semiconductor transition due to the structural change.

## II. EXPERIMENTAL AND CALCULATION DETAILS

The spinel  $\text{Co}_{0.5}\text{Mg}_{0.5}\text{Cr}_2\text{O}_4$  nanoparticle was synthesized using a sol-gel method as reported elsewhere [11]. XRD measurements confirmed that the obtained nanoparticles were single-phase and had a spinel-type structure. Room-temperature (RT) HP powder XRD experiments for  $\text{Co}_{0.5}\text{Mg}_{0.5}\text{Cr}_2\text{O}_4$  were performed at the Beijing Synchrotron Radiation Facility (BSRF, 4W2 beamline), China, with an x-ray wavelength of 0.6199 Å. Pressure was generated with a symmetric diamond-anvil cell (DAC) using a steel gasket and silicon oil as a pressure-transmitting medium. The small difference in the transition pressure can be attributed to the nonhydrostatic effects that prevail beyond 10 GPa [17]. The ruby fluorescence method was employed for pressure calibration [18]. The two-dimensional XRD images were collected with a charge-coupled device (CCD, MAR 165) detector. The two-dimensional ring-type images were first integrated using DIOPAS software [19]. The structural analysis was carried out using FULLPROF software [20]. Raman spectra were collected by a Renishaw InVia Spectrometer system with a laser wavelength of 633 nm with gratings of 1800 l/mm. Silicon oil was used as a pressure-transmitting medium. The HP electrical resistivity of the samples was measured using the standard

four-probe technique in a DAC up to 55 GPa [21]. A mixture of epoxy and cubic boron nitride was used as an insulating layer on the steel gaskets to ensure electrical isolation between the different electrodes. Four platinum electrodes and copper wire were set up to contact the sample in the chamber. No pressure medium was used for the high-pressure electrical resistance measurement. The data were obtained using a 2410-KEITHLEY- source meter.

To gain further insight into the  $\text{Co}_{0.5}\text{Mg}_{0.5}\text{Cr}_2\text{O}_4$  system at low and high pressures, we performed first-principles calculations based on density functional theory (DFT). In our spin-polarized DFT calculations, we used the generalized gradient approximation to the exchange-correlation energy functional proposed by Perdew, Burke, and Ernzerhof (GGA-PBE) [22], as implemented in the VASP package [23,24]. The “Hubbard-U” scheme by Dudarev *et al.* [25] was employed to treat the 3d electrons more appropriately in both the Co and Cr ions; we adopted a  $U_{\text{eff}}$  value of 5.0 eV for the Co ions and 3.7 eV for the Cr ions. This setup provided the best agreement with the lattice parameters found in the experiments. We employed the “projected augmented wave” scheme [26] in our calculations and considered the following electrons as valence states: Mg's  $s^2p^0$ , Co's  $s^1d$  [8], Cr's  $p^6s^1d$  [5], and O's  $s^2p$  [4]. The plane-wave energy cutoff was fixed at 650 eV, and we used a dense Monkhorst-Pack  $\mathbf{k}$ -point grid of  $8 \times 8 \times 8$  to describe the low- $P$  phase ( $Z = 4$ ) and  $11 \times 11 \times 10$  to describe the high- $P$  phase ( $Z = 2$ ). In our atomic relaxations, the tolerance in the atomic forces was set to  $0.01 \text{ eV}/\text{\AA}^{-1}$ . By using these parameters, we obtained total energies that converged to within 0.5 meV per formula unit (f.u.). Additional details on the calculations can be found in the Supplemental Material [27].

## III. RESULTS

### A. Pressure-induced structural transformation

XRD patterns were collected over the pressure range from ambient to 56 GPa. In Fig. 1(a), we present the XRD patterns of  $\text{Co}_{0.5}\text{Mg}_{0.5}\text{Cr}_2\text{O}_4$  at a few representative pressures. The indexes ( $hkl$ ) of the Bragg peaks are marked for the ambient pressure phase. This phase has a cubic structure that belongs to the space group  $Fd\bar{3}m$  [3]. Rietveld analysis provided the initial cell parameter values of the cubic structure, as illustrated in Figs. 1(b) and 1(c).  $\text{Co}_{0.5}\text{Mg}_{0.5}\text{Cr}_2\text{O}_4$  retains the cubic spinel structure up to 28 GPa. Under compression to this pressure, no major structural change was found except a gradual shift of the Bragg peaks toward high angles due to the shrinkage of the unit cell. The peak broadening might be due to the nonhydrostatic conditions, cationic inversion, and a significant number of defects. Upon further compression beyond 28 GPa, shoulders appeared on the left of the main diffraction peaks (220 and 400) of the spinel. These shoulders developed into visible peaks that evolved gradually in intensity with increasing  $P$ , and the existence of a new phase became apparent at about 32 GPa, whereas the spinel gave a modest contribution. We concluded that the cubic spinel started to transform to a new phase above 28 GPa. Both the cubic and HP phase coexisted until 32 GPa, as shown in Fig. 1(a). At 35 GPa, the residual peaks of the cubic spinel phase ( $Fd\bar{3}m$ ) completely disappeared. Rietveld profile fittings were performed with the collected powder diffraction

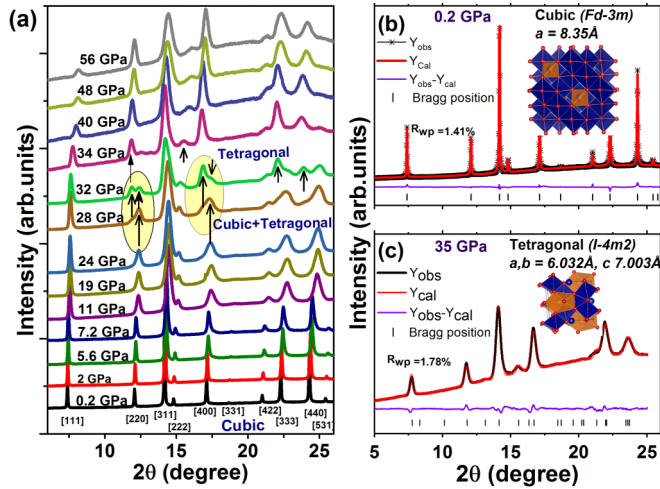


FIG. 1. (a) Angle dispersive XRD patterns for  $\text{Co}_{0.5}\text{Mg}_{0.5}\text{Cr}_2\text{O}_4$  at selected pressures at room temperature.  $\uparrow$  depicts the appearance of the HP phase lines and  $\downarrow$  indicates the disappearance of the LP phase lines. (b) Rietveld refinements for the ambient pressure and new HP phase at 35 GPa.

patterns for both the ambient and HP phases, as shown in Figs. 1(b) and 1(c). We tried to fit the HP diffraction pattern of the new phase by employing different orthorhombic ( $Imma$ ) and tetragonal structures ( $I41/am$ ,  $I\bar{4}m2$ ) based on subgroup considerations and preliminary models. The best agreement between the experimentally obtained pattern and the fitted profile was achieved when the subsequent refinements of the tetragonal ( $I\bar{4}m2$ ) structure were considered, as shown in Figs. 1(b) and 1(c). Detailed information about interatomic positions for both phases is summarized in Table S1 [27]. The HP phase is in good agreement with our theoretical calculations. The new diffraction peaks at  $11.9^\circ$ ,  $15.4^\circ$ ,  $16.7^\circ$ , and  $22.1^\circ$  belong to the tetragonal structure, as illustrated in Fig. 1(a). Thus, we conclude that  $\text{Co}_{0.5}\text{Mg}_{0.5}\text{Cr}_2\text{O}_4$  underwent a phase transition from cubic to tetragonal above 28 GPa. The most dominant factor for this phase transition is the disorder and rearrangements of the octahedral ( $X$  sites) and tetrahedral ( $Y$  sites) [28].

Numerous studies illustrate that most cubic Cr-rich spinels transform to a tetragonal phase upon compression [29,30]. The

profile matching parameters and lattice constant parameters of both the ambient cubic and the HP tetragonal phase as a function of pressure obtained from the full-profile Rietveld refinements are given in Figs. 1(b) and 1(c). This pressure-induced cubic-tetragonal phase transition exhibits a first-order transition, which involved an increase of the material density by approximately 3.0% as a result of the volume collapse. This volume discontinuity can be seen in Fig. 2(a) [14,31]. The unit-cell volume for both the cubic and tetragonal phases decreases continuously as a function of pressure. The pressure-volume data were fitted with the third-order Birch-Murnaghan equation of state (BM-EOS) [30] to determine the elastic parameters:

$$P = \frac{3}{2}K_0 \left[ \left( \frac{V_0}{V} \right)^{7/3} - \left( \frac{V_0}{V} \right)^{5/3} \right] \left[ 1 - \frac{3}{4}(4 - K'_0) \right] \times \left[ \left( \frac{V_0}{V} \right)^{2/3} - 1 \right], \quad (1)$$

where  $P$  and  $V$  are the measured pressure and unit-cell volume respectively,  $K_0$  is the bulk modulus,  $K'_0$  is the first pressure derivative of the bulk modulus, and  $V_0$  is the unit-cell volume at ambient conditions. Calculations offer  $K_0 = 201(4)$ ,  $K'_0 = 6.5(5)$ , and  $V_0 = 582.1(5) \text{ \AA}^3$  for the LP cubic phase. The EOS parameters for the HP phase were obtained by fitting them at the transition pressure. The volume of the HP phase at 35 GPa is  $250(3) \text{ \AA}^3$  (the LP phase has  $Z = 8$  and the HP phase has  $Z = 4$ ), and the bulk modulus  $K = 379(5) \text{ GPa}$  with its derivative  $K' = 4.7(4)$ . These values are comparable with those obtained from the calculations (see the Supplemental Material [27]), and they illustrate that both phases have similar compressibility.  $\text{CoCr}_2\text{O}_4$  and  $\text{MgCr}_2\text{O}_4$  both belong to a normal spinel structure, and both  $\text{Co}^{2+}$  and  $\text{Mg}^{2+}$  occupy the tetrahedral sites, so it is expected that  $K_0$  for  $\text{Co}_{0.5}\text{Mg}_{0.5}\text{Cr}_2\text{O}_4$  have a high magnitude. The bulk modulus and its pressure derivative of  $\text{Co}_{0.5}\text{Mg}_{0.5}\text{Cr}_2\text{O}_4$  determined in this study are also consistent with other Cr-based spinels, as shown in Table I. To analyze the decompression scenario, we have compared the lattice parameters “ $a$ ” for the fully decompressed state and the ambient-pressure cubic sample. We noticed that decompression led to a reversible transformation of the starting  $Fd\bar{3}m$  structure, as shown in Fig. S2 [27]. However, small peak broadening was preserved, possibly due to defects and cationic inversion.

The variations of the experimentally determined lattice parameters of  $\text{Co}_{0.5}\text{Mg}_{0.5}\text{Cr}_2\text{O}_4$  with  $P$  at RT for ambient

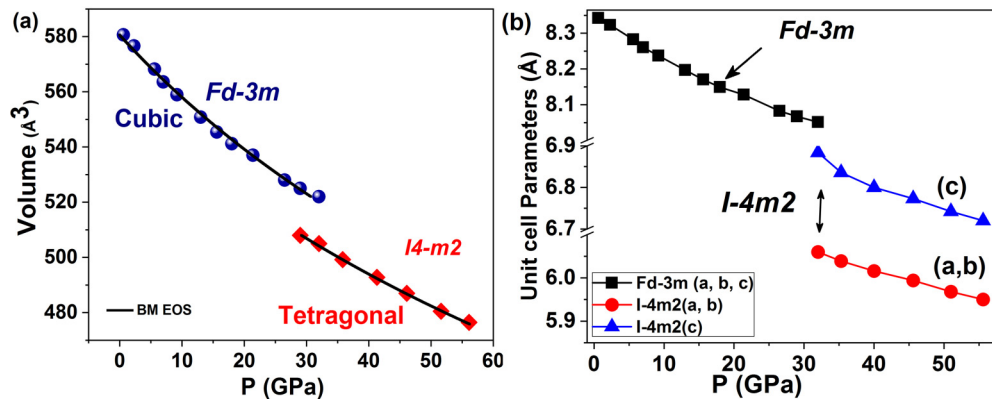


FIG. 2. (a) Unit-cell volume as a function of pressure for the cubic and tetragonal phases. (b) Lattice parameters of  $\text{Co}_{0.5}\text{Mg}_{0.5}\text{Cr}_2\text{O}_4$  as a function of pressure.



TABLE I. Comparison of the experimentally obtained values of the bulk moduli of different Cr-bearing spinels.

Sample composition	$K_0$ (GPa)	References
CoCr <sub>2</sub> O <sub>4</sub>	209	Efthimiopoulos <i>et al.</i> [14]
FeCr <sub>2</sub> O <sub>4</sub>	203	Hearmon <i>et al.</i> [48]
MgCr <sub>2</sub> O <sub>4</sub>	191	Yong <i>et al.</i> [6]
MgCr <sub>2</sub> O <sub>4</sub>	197	Catti <i>et al.</i> [43]
FeCr <sub>2</sub> O <sub>4</sub>	209	Fan <i>et al.</i> [49]
ZnFe <sub>2</sub> O <sub>4</sub>	182	Greenberg <i>et al.</i> [30]
ZnCr <sub>2</sub> O <sub>4</sub>	183	Levy <i>et al.</i> [45]
Co <sub>0.5</sub> Mg <sub>0.5</sub> Cr <sub>2</sub> O <sub>4</sub>	201	This study

and high pressure are summarized in Figs. 1(b) and 1(c) and Fig. S3 [27]. The experimentally obtained lattice parameters are in good agreement with the theoretical predictions. Notice that the compression in the HP tetragonal phase is slightly nonisotropic as the  $c$  axis is the most compressible. The anisotropic behavior is similar to that of the related zircon-type structure [32] and is a direct consequence of the different way in which octahedral and tetrahedral units are connected along different crystallographic directions.

*Ab initio* calculations were carried out to understand the phase transformation of Co<sub>0.5</sub>Mg<sub>0.5</sub>Cr<sub>2</sub>O<sub>4</sub> under pressure. We performed several tests on the low-pressure (LP) spinel phase of Co<sub>0.5</sub>Mg<sub>0.5</sub>Cr<sub>2</sub>O<sub>4</sub>, exploring the effects of the chemical disorder in the sublattice formed by the Mg and Co ions and the magnetic spin ordering on its ground-state enthalpy and structure [22,23]. In our HP calculations, we constrained the Mg/Co ionic disorder and the antiparallel Cr/Co spin arrangement that provided the lowest enthalpy at LP conditions [see Fig. 3(b)]. For details, see the Supplemental Material [27]. We found a tetragonal phase with space group  $I\bar{4}m2$  and  $Z = 2$  (i.e., with a 28-atom unit cell) that appears to be a very good

candidate for the HP phase observed in the experiments [see Figs. 3(a), 3(c), and 3(d)]. Notably, a very similar structure was reported recently by Wheeler *et al.* for MgV<sub>2</sub>O<sub>4</sub> [33]. The lattice parameters of our predicted HP phase obtained at  $P \approx 42$  GPa are  $a = b = 6.0136$  Å and  $c = 6.7612$  Å. The corresponding Wyckoff positions are Co 2d (0.000 00, 0.500 00, 0.750 00), Mg 2b (0.000 00, 0.000 00, 0.500 00), Cr 8i (0.251 14, 0.000 00, 0.876 16), and O 8i (0.295 31, 0.000 00, 0.594 26) and (0.202 25, 0.000 00, 0.158 96). We note that our predicted HP phase does not exhibit any significant Jahn-Teller distortion affecting the CrO<sub>6</sub> octahedron (that is, all the O-Cr-O distances are very similar). In fact, the electronic  $d$ -state configuration that we obtained for the Cr<sup>3+</sup> ions is  $t_{2g}^3 e_g^0$ ; thus, for a Jahn-Teller distortion to develop in the system, the oxidation state of the chromium ions should change first to 2+ to render a high-spin state [34–36]. However, our first-principles analysis based on Bader's charge theory and performed over a wide compression interval (i.e., up to 150 GPa) shows unequivocally that the oxidation state of the Cr ions remains constant and equal to 3+ under high pressure. This finding is fully consistent with the absence of Jahn-Teller distortions in our predicted HP tetragonal phase.

We calculated the zero-temperature enthalpy,  $H = E + PV$ , of the HP spinel and the predicted HP tetragonal phases over the pressure interval  $0 \leq P \leq 100$  GPa. For this, we fitted fourth-order Birch-Murnaghan curves to the set of DFT energies computed for each phase at  $\Delta V/V_0 \approx -1\%$  increments (where  $V_0$  stands for the equilibrium volumes), and we deduced the corresponding zero-temperature enthalpies expressed as a function of pressure [37]. By comparing the enthalpy curves of the two phases, we concluded that the predicted tetragonal phase becomes energetically more favorable than the cubic phase at pressures higher than  $P_t = 42.05$  (5) GPa [Fig. 3(e)]. Such a transition point is in good agreement with the pressure conditions in which a phase transition is experimentally observed in Mg<sub>0.5</sub>Co<sub>0.5</sub>Cr<sub>2</sub>O<sub>4</sub>.

The experimental transition pressure is about 10 GPa smaller than the theoretically predicted pressure. Similar differences between calculated and measured transition pressures have been reported for many oxides [38]. The reasons for such discrepancies have been broadly discussed in the literature, attributing them to nonhydrostatic effects or to mechanical instabilities happening at pressures below the transition pressure determined from the free-energy calculations [39]. Dynamical instabilities should be excluded as the origin of the observed transition pressure difference because calculations found both phases to be dynamically stable in their respective pressure range of stability. We observed that the volume change associated with a transition (2% in theory, 3% experimental) implies a first-order transition. The HP bulk modulus and other theoretical parameters ( $K_0 = 357$ ,  $K'_0 = 3.1$ ,  $V_0 = 248$  Å<sup>3</sup> at 42 GPa) are in good agreement with the experiment and are illustrated in the Supplemental Material with further detailed information of the magnetic spin arrangements and vibrational phonon frequencies for the HP structure [27].

### B. Raman spectroscopy of Co<sub>0.5</sub>Mg<sub>0.5</sub>Cr<sub>2</sub>O<sub>4</sub> under pressure

To study the lattice dynamics of Co<sub>0.5</sub>Mg<sub>0.5</sub>Cr<sub>2</sub>O<sub>4</sub> under pressure, we recorded Raman spectra as a function of  $P$  in the

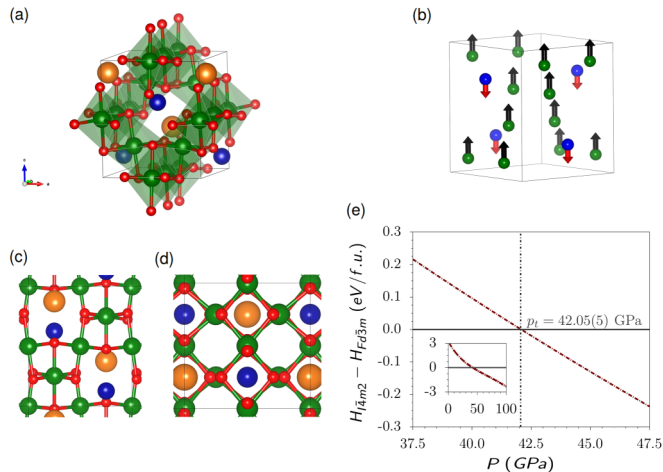


FIG. 3. (a) Atomic structure and (b) magnetic spin arrangement of the predicted HP tetragonal phase. Co and Cr atoms are represented by blue and green spheres, respectively. Mg and O atoms are represented by gold and red spheres, respectively. Atomic magnetic moments are represented by black and red arrows. (c) and (d) Projected views of the HP tetragonal phase along the corresponding  $a$  lattice vector and  $c$  lattice vector, respectively. (e) Enthalpy energy difference of the HP tetragonal and LP cubic phases expressed as a function of pressure.

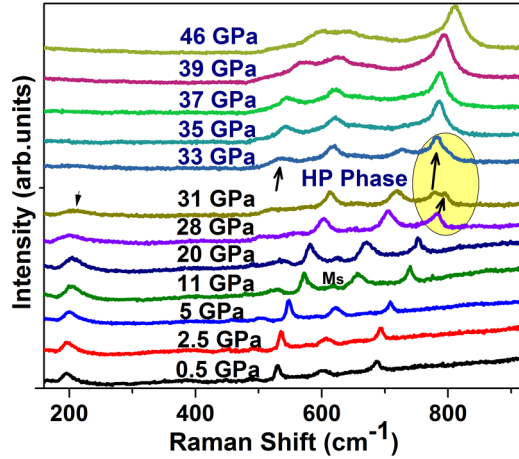


FIG. 4. Raman spectra of  $\text{Co}_{0.5}\text{Mg}_{0.5}\text{Cr}_2\text{O}_4$  at different pressures between 0 and 55 GPa, where the low-frequency Raman modes disappeared at HP.

range of 100–850  $\text{cm}^{-1}$ , as shown in Fig. 4. As a member of the cubic spinels, five Raman-active modes were observed at 193, 480, 524, 612, and 684  $\text{cm}^{-1}$  labeled  $M1$ ,  $M2$ ,  $M3$ ,  $M4$ , and  $M5$  for the relevant Raman modes respectively [3,11]. The factor group analysis predicts that an ideal normal spinel has only five active modes ( $A1g + Eg + 3F2g$ ). The presence of defects, interstitial cations, and vacancies may result in the activation of other phonon modes, which are not predicted by group theory. The lowest-frequency mode,  $M1$ , depends significantly on the tetrahedral cation, and its vibration involves the tetrahedral cation (O-Co/Mg-O) vibration, while the high-frequency modes belong to octahedral vibrations [3,11].

The Raman modes of cubic-spinel  $\text{Co}_{0.5}\text{Mg}_{0.5}\text{Cr}_2\text{O}_4$  show normal behavior upon pressure increase. Our results agree well with previous Raman studies on a similar spinel and unveil the phase transition more clearly. In this study, we observed that (i) all Raman modes shifted to a higher frequency linearly and the ( $M_s \sim 594 \text{ cm}^{-1}$ ) mode became visible around 11 GPa under increasing pressure, (ii) the  $Fd\bar{3}m$  to  $I\bar{4}m2$  transition was due to the appearance of a new Raman mode above 28 GPa, and (iii) the disappearance of the Raman modes and enhanced intensity of new modes occurred above 33 GPa.

Upon compression, the mode labeled  $M_s$  appeared at 11 GPa, which is not included in the Raman-active modes of the  $Fd\bar{3}m$  predicted by group theory. A thorough examination of the Raman spectra revealed that the  $M_s$  band was present at the base of the much more intense  $M3$  mode at ambient conditions and later became visible after compression. Efthimiopoulos *et al.* indicated that the  $M_s$  mode coincides with the  $A1g$  mode of  $\text{Cr}_2\text{O}_3$  and is attributed to local defects. Beyond 28 GPa, new Raman modes appeared at 772 and 530  $\text{cm}^{-1}$  near the cubic-tetragonal phase transition, along with a weakening of the cubic peaks. These Raman modes have not been observed clearly in previous works [14]. Upon further compression ( $P \geq 33$  GPa), the low-frequency Raman modes  $M1$  and  $M2$  eventually disappeared. All these changes demonstrate the rearrangements of ions (tetrahedral  $\leftrightarrow$  octahedral) [28,40]. HP XRD data already confirmed that the structure at this pressure range is tetragonal. Using the calculated HP structure (with

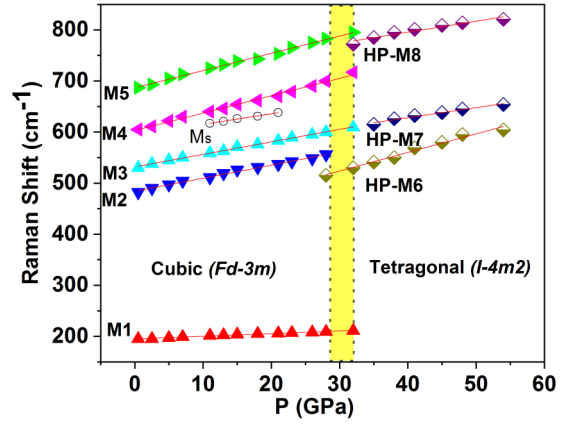


FIG. 5. Pressure dependence of the Raman modes at different pressures between 0 and 55 GPa, where the solid lines show the linear fits corresponding to the specific modes.

the cif), we determined the number of Raman modes ( $6A1 + 3B1 + 7B2 + 10E$ ). We noticed that in the other HP tetragonal spinel structures, only some of the Raman modes could be detected [29]. It is also common that only the strongest modes are observed in the HP phases [29]. Upon further compression, the intensities of the new Raman modes increased with  $P$ . This Raman intensity enhancement can be attributed to resonance effects and the change in conduction. Figure S4 [27] shows the HP Raman spectra of  $\text{Co}_{0.5}\text{Mg}_{0.5}\text{Cr}_2\text{O}_4$  that were collected upon pressure release. However, after the release of  $P$ , some of the Raman modes returned to ambient conditions, indicating that the phase transition is reversible. A part of the HP phase reappeared upon decompression, in agreement with our XRD data.

HP Raman modes of  $\text{Co}_{0.5}\text{Mg}_{0.5}\text{Cr}_2\text{O}_4$  have not been observed in previous works. The pressure dependence of the Raman frequency shifts is plotted in Fig. 5, where considerable changes of  $d\omega/dP$  have been marked by the dotted line region above 28 GPa. Our detailed analysis reflects that with increasing pressure, all phonon modes shift to higher frequencies linearly for both the LP and HP phases. The Grüneisen parameters of the low- and high-pressure regions are calculated and shown in Table II. A comparison of the  $d\omega/dP$  of pure  $\text{CoCr}_2\text{O}_4$ ,  $\text{MgCr}_2\text{O}_4$  with our results shows that the pressure dependence of the Raman-active modes in the three compounds is consistent [40]. Calculations suggest that the observed Raman modes in the HP phase are likely associated with Cr-O vibrations. The Raman frequencies are slightly higher in the calculations (482, 586, and 747  $\text{cm}^{-1}$ ) than in the experiment (414, 549, and 749  $\text{cm}^{-1}$ ), but the pressure coefficients are in good agreement. For more details, see Table S2 [27].

Using the bulk modulus ( $K_0$ ) determined from the x-ray diffraction data, the mode-Grüneisen parameters ( $\gamma$ ) were obtained for both phases with the following equation:  $\gamma = K_0/\omega_0(d\omega/dP)$ , where  $\omega_0$ ,  $P$ , and  $d\omega/dP$  are the frequency of the Raman shift observed at 1 atm, applied pressure, and the pressure-dependent frequency shift of the Raman modes, respectively. The assignment of all the Raman modes in  $\text{Co}_{0.5}\text{Mg}_{0.5}\text{Cr}_2\text{O}_4$  is listed in Table II, along with a summary of the frequencies  $\omega_0$ , pressure coefficient ( $d\omega/dP$ ), and

TABLE II. Observed Raman modes, pressure coefficients ( $d\omega/dP$ ), and calculated Grüneisen parameters of the  $\text{Co}_{0.5}\text{Mg}_{0.5}\text{Cr}_2\text{O}_4$  polymorphs.

Low-pressure spinel phase				High-pressure tetragonal phase			
Raman modes $\omega_0(\text{cm}^{-1})$	$d\omega/dP$ ( $\text{cm}^{-1}/\text{GPa}$ )	$\gamma$	Symmetry	HP observed modes $\omega(\text{cm}^{-1})$	$d\omega/dP$ ( $\text{cm}^{-1}/\text{GPa}$ )	$\gamma$	Symmetry
193	0.517	0.51	(O-Co/Mg-O)				
480	2.56	1.06	Vs (Cr-O), Vs (Co/Mg-O)				
524	2.44	0.92	V (Cr-O)				
$M_s = 594$	2.07	0.7	Vs (Cr-O)	414	3.6	1.8	(Cr-O)
612	3.4	1.13	Vs (Cr-O)	549	1.97	0.74	(Cr-O)
684	1.28	0.42	Vs (Cr-O)	709	2.16	0.65	(Cr-O)

Grüneisen parameter  $\gamma$  of the different modes. The values of the Grüneisen parameters for the cubic and HP tetragonal phases ranged from 0.42 to 1.13 and 0.65 to 1.8, respectively, and they are consistent with previous works in other spinel oxides [38]. The obtained mode Grüneisen parameters can be used to determine the heat capacities and vibrational entropies using the Kieffer model [41]. The high-frequency mode and its association with the Cr-O bonds are explained in detail in the Supplemental Material [27].

### C. Electrical resistivity under high pressure

The pressure-modulated transport characteristics of  $\text{Co}_{0.5}\text{Mg}_{0.5}\text{Cr}_2\text{O}_4$  were obtained up to 56 GPa. Figure 6 depicts the electrical resistivity ( $\rho$ ) of  $\text{Co}_{0.5}\text{Mg}_{0.5}\text{Cr}_2\text{O}_4$  as a function of  $P$  at RT. In the cubic phase,  $\rho$  is  $\sim 10^8 \Omega \text{ cm}$ , two orders of magnitude greater than  $\rho \sim 10^6 \Omega \text{ cm}$  of  $\text{CoCr}_2\text{O}_4$  as Mg partially replaces Co in  $\text{CoCr}_2\text{O}_4$ . Taking into account the RT mobility  $\mu \sim 1.6 \times 10^{-2} \text{ cm}^2/\text{Vs}$  [ $\frac{262}{T} \exp(-0.1/k_B T)$ ], we can estimate the charge density  $n_c \sim 10^{13}/\text{cm}^3$ , which shows the wide-band-gap semiconducting character of  $\text{Co}_{0.5}\text{Mg}_{0.5}\text{Cr}_2\text{O}_4$  at ambient  $P$ . For  $P \leq 10$  GPa,  $\rho$  decreases slowly with pressure in the AB region of Fig. 6. However, at this pressure there is a change in the slope, decreasing the resistivity more rapidly in the BO region of Fig. 6. This change

in the behavior of the resistivity cannot be correlated with any change in the XRD patterns; thus, it is not associated with structural changes. However, it occurs at the same pressure as the  $M_s$  peak appears in the Raman spectra. This suggests that the cation disorder associated with the appearance of  $M_s$  has important consequences for the electrical properties of  $\text{Co}_{0.5}\text{Mg}_{0.5}\text{Cr}_2\text{O}_4$ . From 10 to 30 GPa,  $\rho$  decreases almost linearly with a slope  $d \ln(\rho)/dP \sim -0.051 \pm 0.006 \text{ GPa}^{-1}$  and reaches its lowest value of  $4.5 \times 10^6 \Omega \text{ cm}$  at 30 GPa. The value of resistance at 32 GPa is still  $10^6 \Omega \text{ cm}$ , which suggests that the semiconducting state persists in this pressure range. During compression, connectivity among the grains increases, which weakens the scattering of the grain boundaries and  $\mu$  increases significantly with  $P$ . As a result, resistivity decreases at HP. The interface between the subtle and linear change is not due to a crystal structure change, but it could be due to either disorder in the local structure/local defects or a cation exchange induced by pressure. This result suggests that until the cubic phase survives,  $P$  helps the conduction process and  $\rho$  decreases at BO. For  $P > 35$  GPa,  $\rho$  started to increase smoothly up to 55 GPa in the OC region and reached maximum resistance  $8.2 \times 10^7 \Omega \text{ cm}$ , basically changing about two orders of magnitude. The rate of change of  $\rho$  at OC is  $d \ln(\rho)/dP \sim 0.0434 \pm 0.021 \text{ GPa}^{-1}$ . Our Raman and XRD data show that the HP tetragonal phase started to evolve above 28 GPa, and the HP phase is fully formed at 35 GPa, where the increase of resistivity (decrease of electrical conductivity) is observed as pressure increases. The small difference in the transition pressure between the XRD and transport measurements could be attributed to their different hydrostaticity.

Since the studied material has a wide band gap, the decrease of conductivity cannot be correlated with changes induced by pressure in the band-gap energy. The most reasonable hypothesis to explain the observed phenomenon is that the increase in resistivity is due to the formation of internal defects accompanying the pressure-induced structural transformation [42]. These defects are expected to compensate the material and reduce the carrier mobility. At 55 GPa, the tetragonal phase is less conductive than at 35 GPa and almost equally conductive to the ambient phase with a rough estimation of  $n_c \sim 10^{15}/\text{cm}^3$  and  $10^{13}/\text{cm}^3$  for 35 and 55 GPa, respectively. In the decompression cycle, a part of  $\rho$  was recovered due to the mixture of the HP and LP phases but failed to come back at the original phase. In fact, the defects did not revert after

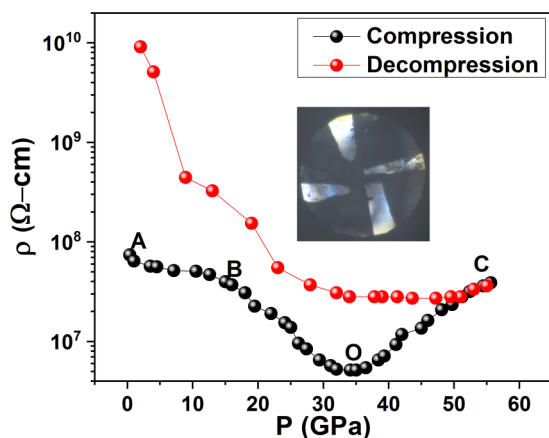


FIG. 6. Electrical resistance behavior of  $\text{Co}_{0.5}\text{Mg}_{0.5}\text{Cr}_2\text{O}_4$  as a function of pressure at RT.

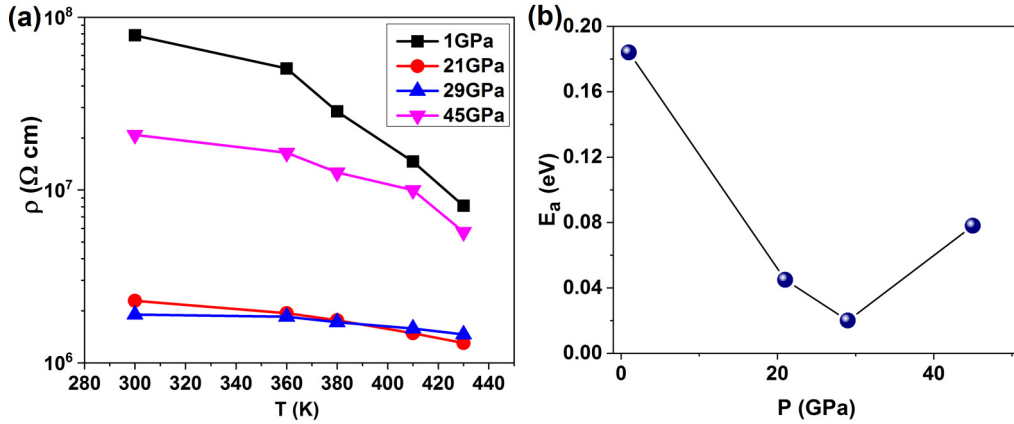


FIG. 7. (a) Isobaric temperature-dependent resistivity of the few representative pressure values. (b) The pressure dependence of the activation energy  $E_a$  obtained from the slope of  $\ln \rho$  and  $1/k_B T$ .

reducing the pressure. More defects can certainly be created when the ambient pressure phase is recovered and leads to a higher resistivity in the recovered sample.

To better understand our transport results, we also measured resistivity as a function of temperature at a few fixed pressures, and the results are shown in Fig. 7. We analyzed the resistivity decrease with increasing temperature. For the cubic phase, the negative slopes of temperature-dependent resistivity are  $d \ln(\rho)/dT \sim 0.0075, 0.0023$ , and  $0.0011$  at 1, 21, and 29 GPa, respectively. We observed a minimum  $d \ln(\rho)/dT$  at 29 GPa. For the tetragonal phase,  $\rho$  increases with the slope  $d \ln(\rho)/dT \sim -0.0048$  for  $P \sim 40$  GPa. In both phases, at a particular pressure, the resistivity decreases gradually with increasing temperature, confirming the semiconducting behavior of both phases. Using the Arrhenius equation,  $\rho \sim \exp(\frac{E_a}{2k_B T})$ , we plotted the activation energy as a function of pressure to further investigate the sample, as shown in Fig. 7(b).  $E_a$  decreases rapidly with increasing pressure in the low-pressure phase, and after the transition it increases, which is consistent with the resistivity increase. All these results suggest that a pressure-induced semiconductor-semiconductor transition occurred during the structural change.

#### IV. DISCUSSIONS

Our XRD experiment illustrates that a cubic-tetragonal phase transition for  $\text{Co}_{0.5}\text{Mg}_{0.5}\text{Cr}_2\text{O}_4$  develops above 28 GPa, in good agreement with the Raman spectroscopic and transport measurements. The reliability of the cubic-tetragonal transition is supported by the consistency between the theoretical and experimental results. Previous high-pressure studies on Cr-based spinel oxides by Wang *et al.* and Efthimiopoulos *et al.* [14,40] also proposed a cubic-to-tetragonal transition, with phases coexisting over a wide range of pressure from 14 to 30 GPa. Theoretical calculations anticipated the decomposition of the  $\text{MnCr}_2\text{O}_4$ ,  $\text{ZnCr}_2\text{O}_4$ , and  $\text{MgCr}_2\text{O}_4$  spinel into its oxides upon compression [43]. Such decomposition was only found under HP-HT conditions at temperatures higher than 1000 °C [44]. Our experiments and calculations did not support decomposition, but they show that  $\text{Co}_{0.5}\text{Mg}_{0.5}\text{Cr}_2\text{O}_4$  has different behavior from other spinel oxides, similar to that reported recently by Wheeler *et al.* for  $\text{MgV}_2\text{O}_4$  [33]. Furthermore,

Levy *et al.* and Yong *et al.* did not verify decomposition at room temperature in their experimental studies on  $\text{ZnCr}_2\text{O}_4$  and  $\text{MgCr}_2\text{O}_4$ , respectively [6,45]. Our theoretical results agree well with our experiments, providing a good description of the crystal and electronic structure at all the studied pressures.

Efthimiopoulos *et al.* suggest that the structural modification found by them in  $\text{CoCr}_2\text{O}_4$  is mainly driven by magnetic effects induced under pressure. According to our calculations, this is not the case for the cubic-tetragonal transition of our sample. In our DFT calculations, we did not observe any appreciable change in the magnetic structure of the material during the structural pressure-induced phase transition (that is, the total magnetic moments in the Co and Cr ions remain constant, at 2.7 and 2.9  $\mu_B$ , respectively, as well as their relative orientations). Consequently, we cannot infer any pressure-induced enhancement of the magnetic interactions. In contrast, DFT calculations found that the phase transition occurs to minimize the energy of the electronic interaction of the system. This is, in part, related to a small change of the occupation of the  $d$  orbitals in Co and Cr, which has generally been attributed to an  $s > d$  electron transfer in the material when it is under pressure. However, there is no change in the oxidation state of Cr after the transition, and the HP phase does not display a Jahn-Teller distortion in the  $\text{CrO}_6$  octahedron.

Signatures of the pressure-induced structural phase transition are also expected in the pressure evolution of the electronic excitations degenerated from transport measurements. Resistivity measurements reveal a significant correlation with the structural transitions in our  $\text{Co}_{0.5}\text{Mg}_{0.5}\text{Cr}_2\text{O}_4$  above 28 GPa. The resistance increases anomalously at a similar rate to its decrease in the cubic phase. This increase in resistivity under compression is anomalous and rarely encountered in the spinel system, especially in Cr-based spinel. Other chromates, such as  $\text{FeCr}_2\text{O}_4$ , exhibit a usual decrease in resistance at high pressures, and no sign of an increase in resistivity was observed up to 70 GPa [16]. The changes we observed in our resistivity behavior cannot be caused by changes in the electronic structure, in particular by an enlargement of the band gap as the pressure is increased in the high-pressure structural polymorph. Such a phenomenon would only be detectable in small-band-gap ( $<1$  eV) materials at RT. Therefore, the increase in resistivity is possibly due to the formation of



internal defects accompanying the pressure-induced structural transformation [46]. The formation of such defects could considerably lower the free-carrier mobility leading to the observed increase of the resistivity. A first-order reconstructive transition can lead to the formation of a larger number of defects. It is known that the formation of defects can lead to an increase in resistance accompanying the structural transition under compression, as observed in several semiconducting systems [42,47]. The formation of crystal defects by applied pressure leads to carrier trapping and increased scattering at the grain boundaries, both of which will decrease carrier concentration and mobility. Indeed, the substitution of  $\text{Co}^{2+}$  with a smaller ion of  $\text{Mg}^{2+}$  in  $\text{Co}_{0.5}\text{Mg}_{0.5}\text{Cr}_2\text{O}_4$  can introduce a cationic vacancy in the crystal. Such vacancy defects can be enhanced by the structural phase transformation. As a result, the resistivity is increased at higher pressure.

## V. CONCLUSION

In summary, we have explored the structural, vibrational, and electronic behavior of Mg-doped Cr-rich spinel  $\text{Co}_{0.5}\text{Mg}_{0.5}\text{Cr}_2\text{O}_4$  up to 55 GPa using a combination of experimental and *ab initio* methods. The structural transition  $Fd\bar{3}m - I\bar{4}m2$  appeared above 28 GPa and was accompanied by a modification in the vibrational and electronic properties of the sample, as revealed by our Raman and electrical studies.

Our DFT calculations confirm this first-order phase transition and support our experimental results. The tetragonal high-pressure phase hinders the conduction behavior, while the cubic phase supported conductivity behavior with compression. The behavior of  $\text{Co}_{0.5}\text{Mg}_{0.5}\text{Cr}_2\text{O}_4$  is compared with that of other spinel-type oxides. Our HP resistivity measurements confirm that the low- and high-pressure phases are wide-band-gap semiconductors, indicating a semiconductor-semiconductor transition due to the structural change.

## ACKNOWLEDGMENTS

This work was supported by NSAF (Grant No. U1530402). C.C. acknowledges support from the Australian Research Council through the Future Fellowship funding scheme (Project No. FT140100135). Computational resources and technical assistance were provided by the Australian Government and the Government of Western Australia through Magnus under the National Computational Merit Allocation Scheme and The Pawsey Supercomputing Centre. D.E. thanks the Spanish Ministerio de Economía y Competitividad (MINECO), the Spanish Research Agency (AEI), and the European Fund for Regional Development (FEDER) under Grants No. MAT2016-75586-C4-1-P and No. MAT2015-71070-REDC (MALTA Consolider) for financially supporting this research. J.L. thanks the National Natural Science Foundation of China (Grant No. 21673215).

- 
- [1] C.-W. Nan, M. I. Bichurin, S. Dong, D. Viehland, and G. Srinivasan, *J. Appl. Phys.* **103**, 031101 (2008).
  - [2] Y. Yamasaki, S. Miyasaka, Y. Kaneko, J. P. He, T. Arima, and Y. Tokura, *Phys. Rev. Lett.* **96**, 207204 (2006).
  - [3] P. Choudhary and D. Varshney, *J. Alloys Compd.* **725**, 415 (2017).
  - [4] R. Hashemi, *Int. J. Eng. Sci.* **103**, 59 (2016).
  - [5] A. K. Karklit, S. A. Stegantsev, and E. V. Petrova, *Refractories* **11**, 786 (1970).
  - [6] W. Yong, S. Botis, S. R. Shieh, W. Shi, and A. C. Withers, *Phys. Earth Planet. Inter.* **196-197**, 75 (2012).
  - [7] S. C. Sharma and S. Gopal, *Trans. Ind. Ceram. Soc.* **53**, 116 (1994).
  - [8] K. C. Patil, *Chemistry of Nanocrystalline Oxide Materials: Combustion Synthesis, Properties and Applications* (World Scientific, Singapore, 2008).
  - [9] S. Rahman, S. Samanta, D. Errandonea, S. Yan, K. Yang, J. Lu, and L. Wang, *Phys. Rev. B* **95**, 024107 (2017).
  - [10] N. Inagaki, *Plasma Surface Modification and Plasma Polymerization* (Taylor & Francis, London, 1996).
  - [11] M. Kamran, A. Ullah, S. Rahman, A. Tahir, K. Nadeem, M. Anis ur Rehman, and S. Hussain, *J. Magn. Magn. Mater.* **433**, 178 (2017).
  - [12] C. Pankaj and V. Dinesh, *Mater. Res. Express* **4**, 076110 (2017).
  - [13] H. Lü, W. Ma, H. Zhao, J. Du, and X. Yu, *Mater. Manuf. Proc.* **26**, 1233 (2011).
  - [14] I. Efthimiopoulos, Z. T. Y. Liu, S. V. Khare, P. Sarin, T. Lochbiler, V. Tsurkan, A. Loidl, D. Popov, and Y. Wang, *Phys. Rev. B* **92**, 064108 (2015).
  - [15] H. K. Mao and P. M. Bell, *Science* **176**, 403 (1972).
  - [16] W. M. Xu, G. R. Hearne, S. Layek, D. Levy, J. P. Itié, M. P. Pasternak, G. K. Rozenberg, and E. Greenberg, *Phys. Rev. B* **95**, 045110 (2017).
  - [17] D. Errandonea, Y. Meng, M. Somayazulu, and D. Häusermann, *Physica B* **355**, 116 (2005).
  - [18] H. K. Mao, J. Xu, and P. M. Bell, *J. Geophys. Res.* **91**, 4673 (1986).
  - [19] C. Prescher and V. B. Prakapenka, *High Press. Res.* **35**, 223 (2015).
  - [20] J. Rodríguez-Carvajal, *Physica B* **192**, 55 (1993).
  - [21] S. Samanta, Q. Li, B. Cheng, Y. Huang, C. Pei, Q. Wang, Y. Ma, and L. Wang, *Phys. Rev. B* **95**, 045135 (2017).
  - [22] J. P. Perdew, K. Burke, and M. Ernzerhof, *Phys. Rev. Lett.* **78**, 1396 (1997).
  - [23] G. Kresse and J. Furthmüller, *Phys. Rev. B* **54**, 11169 (1996).
  - [24] G. Kresse and D. Joubert, *Phys. Rev. B* **59**, 1758 (1999).
  - [25] S. L. Dudarev, G. A. Botton, S. Y. Savrasov, C. J. Humphreys, and A. P. Sutton, *Phys. Rev. B* **57**, 1505 (1998).
  - [26] P. E. Blöchl, *Phys. Rev. B* **50**, 17953 (1994).
  - [27] See Supplemental Material at <http://link.aps.org/supplemental/10.1103/PhysRevB.97.174102> for (i) calculation details; (ii) decompression of HP XRD; (iii) axial compression as a function of pressure; (iv) interatomic positions and relevant parameters of both phases; (v) calculated HP Raman modes; (vi) detailed information on the splitting of the Raman modes; (vii) decompression of HP Raman spectroscopy; (viii) Raman spectra of silicon oil along with  $\text{Co}_{0.5}\text{Mg}_{0.5}\text{Cr}_2\text{O}_4$  spectra; and (ix) TEM images of  $\text{Co}_{0.5}\text{Mg}_{0.5}\text{Cr}_2\text{O}_4$ .



- [28] Z. Wang, S. K. Saxena, P. Lazor, and H. S. C. O'Neill, *J. Phys. Chem. Solids* **64**, 425 (2003).
- [29] Z. Wang, R. T. Downs, V. Pischedda, R. Shetty, S. K. Saxena, C. S. Zha, Y. S. Zhao, D. Schiferl, and A. Waskowska, *Phys. Rev. B* **68**, 094101 (2003).
- [30] E. Greenberg, G. K. Rozenberg, W. Xu, R. Arielly, M. P. Pasternak, A. Melchior, G. Garbarino, and L. S. Dubrovinsky, *High Press. Res.* **29**, 764 (2009).
- [31] S. Ferrari, R. S. Kumar, F. Grinblat, J. C. Apesteguy, F. D. Saccone, and D. Errandonea, *Solid State Sci.* **56**, 68 (2016).
- [32] O. Gomis, B. Lavina, P. Rodríguez-Hernández, A. Muñoz, R. Errandonea, D. Errandonea, and M. Bettinelli, *J. Phys.: Condens. Matter* **29**, 095401 (2017).
- [33] E. M. Wheeler, B. Lake, A. T. M. Nazmul Islam, M. Reehuis, P. Steffens, T. Guidi, and A. H. Hill, *Phys. Rev. B* **82**, 140406(R) (2010).
- [34] S. H. Lee, C. Broholm, T. H. Kim, W. Ratcliff, and S. W. Cheong, *Phys. Rev. Lett.* **84**, 3718 (2000).
- [35] A. Kyono, S. A. Gramsch, Y. Nakamoto, M. Sakata, M. Kato, T. Tamura, and T. Yamanaka, *Am. Mineral.* **100**, 1752 (2015).
- [36] O. Tchernyshyov, *Phys. Rev. Lett.* **93**, 157206 (2004).
- [37] F. Birch, *Phys. Rev.* **71**, 809 (1947).
- [38] J. López-Solano, P. Rodríguez-Hernández, A. Muñoz, O. Gomis, D. Santamaría-Perez, D. Errandonea, F. J. Manjón, R. S. Kumar, E. Stavrou, and C. Raptis, *Phys. Rev. B* **81**, 144126 (2010).
- [39] D. Errandonea, O. Gomis, D. Santamaría-Perez, B. García-Domene, A. Muñoz, P. Rodríguez-Hernández, S. N. Achary, A. K. Tyagi, and C. Popescu, *J. Appl. Phys.* **117**, 105902 (2015).
- [40] Z. Wang, H. S. C. O'Neill, P. Lazor, and S. K. Saxena, *J. Phys. Chem. Solids* **63**, 2057 (2002).
- [41] A. M. Hofmeister and H.-k. Mao, *Proc. Natl. Acad. Sci. (USA)* **99**, 559 (2002).
- [42] D. Errandonea, A. Segura, D. Martínez-García, and V. Muñoz-San Jose, *Phys. Rev. B* **79**, 125203 (2009).
- [43] M. Catti, F. F. Fava, C. Zicovich, and R. Dovesi, *Phys. Chem. Miner.* **26**, 389 (1999).
- [44] T. Ishii, H. Kojitani, K. Fujino, H. Yusa, D. Mori, and Y. Inaguma, *Am. Mineral.* **100**, 59 (2015).
- [45] D. Levy, V. Diella, A. Pavese, M. Dapiaggi, and A. Sani, *Am. Mineral.* **90**, 1157 (2005).
- [46] D. Errandonea, E. Bandiello, A. Segura, J. J. Hamlin, M. B. Maple, P. Rodriguez-Hernandez, and A. Muñoz, *J. Alloys Compd.* **587**, 14 (2014).
- [47] D. Errandonea, A. Segura, J. F. Sánchez-Royo, V. Muñoz, P. Grima, A. Chevy, and C. Ulrich, *Phys. Rev. B* **55**, 16217 (1997).
- [48] R. F. S. Hearmon, *Landolt-Börnstein* (Springer, Berlin, 1984), p. 559.
- [49] D. Fan, W. Zhou, C. Liu, Y. Liu, X. Jiang, F. Wan, J. Liu, X. Li, and H. Xie, *J. Mater. Sci.* **43**, 5546 (2008).